Journal of Materials Chemistry A

RSC Publishing

COMMUNICATION

View Article Online
View Journal | View Issue

Cite this: J. Mater. Chem. A, 2013, 1, 7306

Received 28th March 2013
Accepted 2nd May 2013

DOI: 10.1039/c3ta11262d

www.rsc.org/MaterialsA

In situ self-catalyzed formation of core–shell $LiFePO_4$@CNT nanowires for high rate performance lithium-ion batteries†

Jinli Yang,[a] Jiajun Wang,[a] Yongji Tang,[ab] Dongniu Wang,[ab] Biwei Xiao,[a] Xifei Li,[a] Ruying Li,[a] Guoxian Liang,[c] Tsun-Kong Sham[b] and Xueliang Sun*[a]

In situ **self-catalyzed core–shell $LiFePO_4$@CNT nanowires can be fabricated by a two-step synthesis, where one-dimensional $LiFePO_4$ nanowires with a diameter of 20–30 nm were encapsulated into CNTs, and 3D conducting networks of CNTs were obtained from *in situ* carbonization of a polymer. $LiFePO_4$@CNT nanowires deliver a capacity of 160 mA h g^{-1} at 17 mA g^{-1}, and 65 mA h g^{-1} at 8500 mA g^{-1} (50 C, 1.2 minutes for charging and 1.2 minutes for discharging).**

$LiFePO_4$ with an olivine structure is an attractive cathode material applied in lithium ion batteries (LIBs) because of its low cost, high thermal and chemical stability, and acceptable operating voltage (3.4 V *versus* Li^+/Li).[1] The poor electronic conductivity ($\sim 10^{-9}$ S cm^{-1}) of $LiFePO_4$ is usually circumvented by carbon coating on the surface of $LiFePO_4$.[2,3] The current focus for $LiFePO_4$ applied in large-size batteries (electric vehicles and hybrid electrical vehicles) is on ultrafast battery discharge. This goal can be achieved by decreasing the size of $LiFePO_4$.[4,5] According to the formula,[6] $L = \sqrt{D\tau}$ (where D is the diffusion coefficient, τ is the diffusion time and L is the diffusion distance), the short diffusion lengths could shorten the diffusion time of Li ions in $LiFePO_4$ during the intercalation–deintercalation process and the relatively high surface area of the nano-sized particles also enables fast charge transfer.[7,8] Unfortunately, more undesirable chemical reactions occurring at the electrolyte–electrode interface layer will produce HF, which attacks the surface of $LiFePO_4$, leading to poor cycle performance.[4d] One effective way to eliminate this problem is complete carbon coating.[4b,9–11] Insufficient use of $LiFePO_4$ occurs in places where carbon is unattached during the intercalation process, thus resulting in polarization of the electrode.[10] Full carbon coating plays a bifunctional role (conductivity improvement and protection barrier), ensuring that $LiFePO_4$ particles get electrons from all directions, avoiding direct contact with the electrolyte, thus alleviating polarization and improving cycle life.[4d,11]

Another strategy is hierarchical nanostructure design.[12–17] An electrode consisting of carbon-coated, high-crystalline $LiFePO_4$ in the nanoscale with three dimensional (3D) conductive networks is desired for high power LIBs.[14,15] Wu *et al.*[12] recently synthesized hierarchical carbon-coated $LiFePO_4$ nanoplates, which possess a unique geometrical structure that is helpful in facilitating the fast transport of mass and charge, hence they exhibit considerable discharge capacity and rate capability. In the case of carbon, carbon nanotubes (CNTs) are superior conducting materials for hybridization of active materials.[14] Incorporation of CNTs into $LiFePO_4$ has demonstrated improved specific capacity and rate capability of the composites.[4c,16] Nevertheless, in these composites, CNTs were randomly dispersed into micro-sized $LiFePO_4$, hence the ways of combination of $LiFePO_4$ and CNTs are limited.

Herein we synthesized, for the first time to our knowledge, one-dimensional $LiFePO_4$ nanowires with a diameter of 20–30 nm encapsulated into CNTs (LFP@CNTs); 3D conducting networks of CNTs were simultaneously obtained during the solid state reaction. One-dimensional $LiFePO_4$ nanowires reduce the diffusion path of Li ions, while the CNT shell ensures a full coating and a fast electron conduction path. By combining the advantages of one-dimensional core–shell LFP@CNTs and 3D CNT conducting networks, a hierarchical nanostructure design of electrode materials for high power and high energy LIBs can be realized.

LFP@CNT core–shell nanowires were fabricated by a two step process: (1) a sol–gel route to get one-dimensional $LiFePO_4$ nanowire precursor; (2) a solid state reaction to obtain core–shell high-crystalline LFP@CNT nanowires and CNT networks by *in situ* carbonization of polymers. The schematic drawing of the synthetic procedure is demonstrated in Scheme 1. First,

[a]Department of Mechanical and Materials Engineering, Western University, London, Ontario N6A 5B9, Canada. E-mail: xsun9@uwo.ca

[b]Department of Chemistry, Western University, London, Ontario N6A 5B9, Canada

[c]Clariant (Canada), 1475, Marie-Victorin, St-Bruno, Quebec J3V 6B7, Canada

† Electronic supplementary information (ESI) available: Experimental part, selected-area electron diffraction pattern, SEM images, TEM images, Raman spectrum and charge–discharge galvanostatic curves for different cycles of LFP@CNT composites. See DOI: 10.1039/c3ta11262d

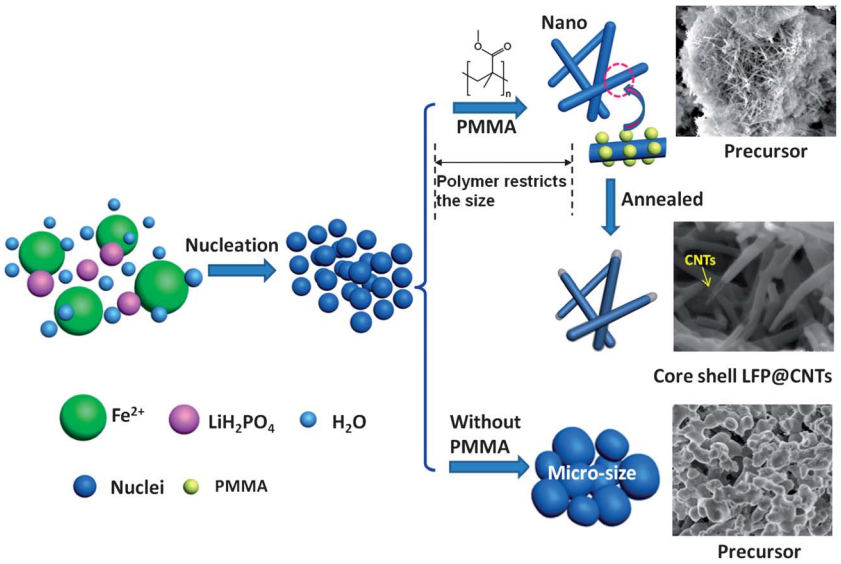

Scheme 1 Schematics to illustrate the synthetic procedure of the LFP@CNT nanocomposites.

one-dimensional nanowire structure is obtained by polymerization of polymethylmethacrylate (PMMA) during the sol–gel process. It is also noted that the PMMA polymer can restrict the size of the $LiFePO_4$ precursor. This is caused by *in situ* polymerization of PMMA on the outer surface of the generated $LiFePO_4$ precursor precipitate, followed by formation of a shell to restrict the growth of $LiFePO_4$.[9] In contrast, micro-sized particles are obtained without PMMA. Subsequent heat treatment at 700 °C for 10 h under argon leads to formation of core–shell LFP@CNT nanowires and the CNT network (LFP@CNTs-10 h). During this step, Fe^{2+} provided by the composites facilitates the formation of the CNT shells[18] and network through PMMA carbonization. Meanwhile, the CNT shell restricts the *in situ* crystallite growth of $LiFePO_4$ nanowires.

The scanning electron microscopy (SEM) image shown in Fig. 1a suggests that the one-dimensional core–shell LFP@CNT nanowires can be created on a large scale basis. The corresponding magnified SEM images shown in Fig. 1b indicate that the typical diameter of the prepared LFP@CNT nanowires is in the range of 20–30 nm, and the needle-like $LiFePO_4$ nanowires are encapsulated into CNTs, which are *in situ* generated by carbonization of the PMMA polymer. A transmission electron microscopy (TEM) image (Fig. 1c) further demonstrates the core–shell structure of LFP@CNTs-10 h. It is interesting to note that LFP@CNT nanowires are inter-connected by the 3D CNT network (indicated by arrows), which results from *in situ* carbonization of PMMA (more images are shown in Fig. S1†). The electrons can easily reach the LFP@CNT nanowires through the 3D conducting network. The specific BET surface area of the LFP@CNT nanowires is 34.3 $m^2\ g^{-1}$.

A high-resolution TEM image (Fig. 1d) clearly reveals that a transparent CNT shell with a thickness of 3 nm encapsulates $LiFePO_4$ nanowire, and the number of walls is around 5–8 layers for typical CNTs as shown in Fig. S1.† Lithium ions can easily diffuse in the framework of $LiFePO_4$ through the thin carbon shell during the intercalation and deintercalation process.[19] The CNT shell has an approximate diameter of 15 nm and less near the tip. The lattice fringes with a width of 0.18 nm correspond to the (131) plane of $LiFePO_4$. Selected-area electron diffraction (SAED) patterns suggest that the fabricated $LiFePO_4$ nanowires are highly crystalline (Fig. S2†). Energy-dispersive X-ray (EDX) line scanning (Fig. 1e) of a single LFP@CNT nanowire (inset in Fig. 1e) shows the evidence for a core–shell structure with the carbon signal peak at the shell of the nanowire and the Fe, P and O signal peaks at the core of the nanowire. As illustrated in Fig. 1f, Li ions could easily diffuse in and out of the high-crystalline LFP@CNT nanowire, due to its nanometer scale dimension and large surface area. Electrons could also be effectively supplied into the $LiFePO_4$ core through the CNT shell and the 3D CNT networks during cycling.

The crystallite size of LFP@CNTs-10 h is similar to the size of its precursor (Fig. S3†), indicating that the formed CNT shell effectively restricts the crystallite growth of $LiFePO_4$. As we know, carbon can be consumed by the residual oxygen in the argon-filled tube furnace during the calcination process. In order to further investigate the protective effect of the CNT shell, we performed the annealing process at 5 h and 20 h. It is noted that a core–shell nanowire structure can be obtained for the 5 h treated sample (LFP@CNTs-5 h), while for 20 h annealed sample (LFP@CNTs-20 h), $LiFePO_4$ nanowires were cracked into nanorods and agglomerated within a diameter of 50–100 nm (Fig. S4†). The HRTEM images show a typical example of core–shell LFP@CNT nanowires annealed for different times (Fig. 2). It is clearly observed that an amorphous CNT shell (5 h) evolves into a graphitized CNT shell (10 h) and the CNT tip (20 h) disappears in the core–shell structure, which is consistent with the TGA results (Fig. 3b). After calculation,[4a,20] the carbon contents in LFP@CNTs-5 h, LFP@CNTs-10 h and LFP@CNTs-20 h are about 4.1 wt%, 3.9 wt% and 3.1 wt%, respectively, providing evidence for carbon loss when prolonging the annealing time. Graphitized carbon shown in the Raman spectrum (Fig. S5†) guarantees high electronic transfer

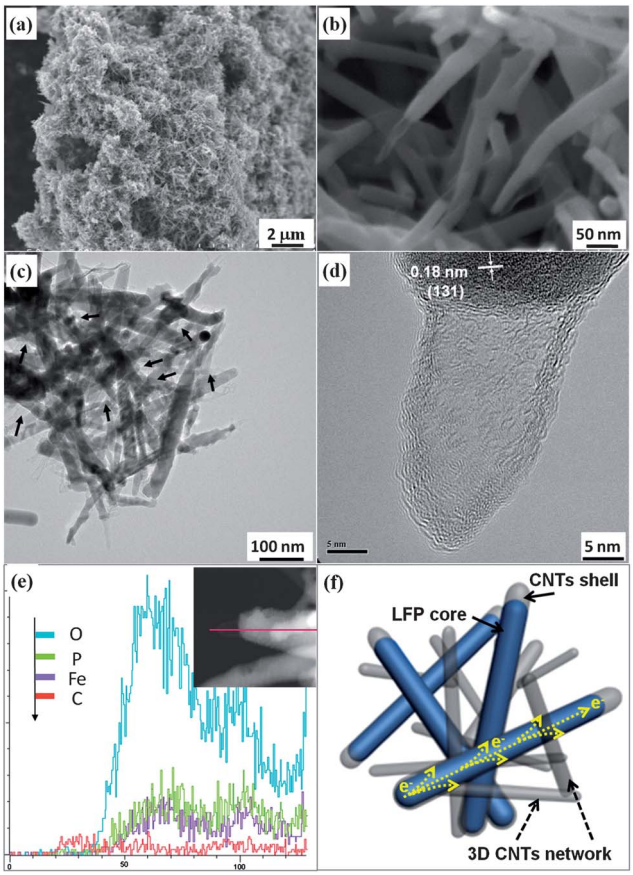

Fig. 1 (a and b) SEM images of the as-prepared needle-like LFP@CNTs. (c) TEM image of the fabricated core–shell nanowires, and (d) the corresponding HRTEM image of a LFP@CNT nanowire. (e) EDX line scanning of a LFP@CNT core–shell nanowire. HRTEM image of a single LFP@CNT nanowire (inset). (f) Schematic illustration of LFP@CNT core–shell nanowires.

capability of the LFP@CNT composites.[21] The XRD patterns of the prepared samples can be indexed as olivine $LiFePO_4$ (JCPDS no. 40-1499), and the precursor is completely transformed into $LiFePO_4$ (Fig. 3a), indicating that high-crystalline and pure $LiFePO_4$ was obtained in the calcination step.

In order to investigate (i) the interaction (chemical bonding) between the CNT shell and $LiFePO_4$ core and (ii) the local chemistry environment of elemental Fe in LFP@CNT composites, C K-edge and Fe K-edge X-ray absorption near edge structure (XANES) spectra were studied (Fig. 3c and d). The Fe K-edge XANES spectra exhibit a pre-edge and an edge jump (Fig. 3c). The pre-edge peak is centered at the lower energy side of the sharply rising absorption edge (white line), corresponding to the 1s to 3d electronic transition of Fe.[22] All of the LFP@CNT composites exhibited an edge feature characteristic of Fe(II) and a distinct increased white line located at ~7126 eV, indicating an Fe bivalence feature with some depleted p character with increasing annealing time.[22,23] The gradually increasing resonance at ~7141 eV indicates the improved crystallinity of the composites when prolonging the annealing time. Three regions of resonance in the C K-edge XANES spectra can be observed (Fig. 3d). Two patterns located at ~285 eV and 291 eV (at a and c positions) correspond to graphitic π* and σ* transitions, respectively.[24] The presence of graphitic π* and σ* transitions implies that the graphitic framework exists in LFP@CNT nanocomposites. The most interesting feature in the spectra is the obvious resonance at ~288 eV (at the b position), which arises from the oxygen containing functional group of carboxylate bonding among other C–O single bond functionalities.[24a] Many groups attribute this resonance to the chemical bonding between active materials and carboxylate groups.[24b,25] The intensity of peak b from LFP@CNTs-20 h is lower than that of the other two composites, indicating the weakened carboxylate bonding in the composites. This is further proved by the increase in the intensity of the π* resonance, pending no

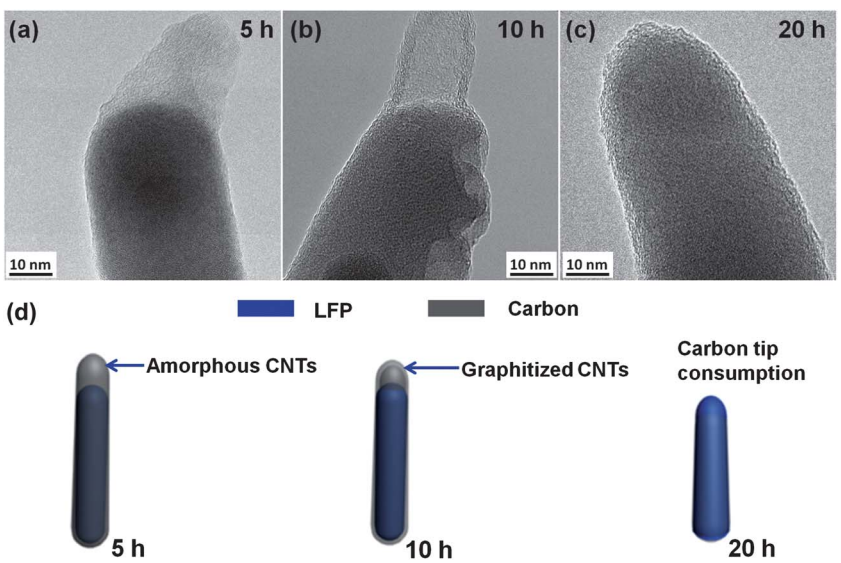

Fig. 2 TEM images of LFP@CNT composites annealed for different times: (a) 5 h, (b) 10 h, (c) 20 h. (d) Schematics of morphology evolution.

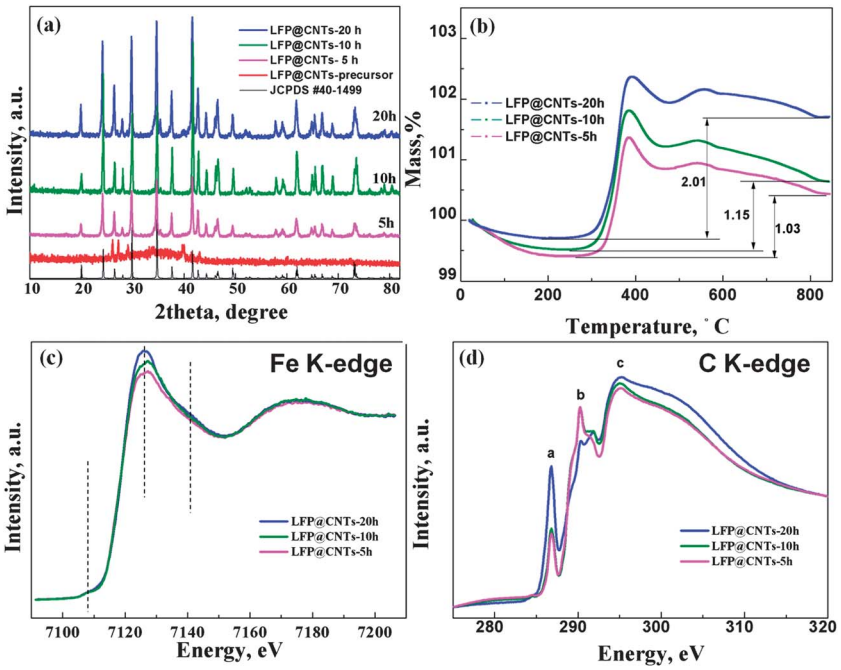

Fig. 3 XRD patterns (a) and TGA curves (b) of LFP@CNT composites. Normalized XANES spectra for LFP@CNT composites: (c) Fe K-edge; (d) C K-edge.

countervailing arguments of texture for these random powder samples; this observation strongly indicates that a more ordered graphitic situation is restored. Considering that carboxylate bonding is related to the interaction between the CNT shell and $LiFePO_4$ core, this phenomenon provides direct spectroscopic evidence that the interaction between the CNT shell and $LiFePO_4$ core is stronger in LFP@CNTs-10 h than LFP@CNTs-20 h.

Fig. 4 shows the electrochemical performance of the LFP@CNT nanocomposite. A couple of redox peaks are observed for the three cyclic voltammetry (CV) curves (1^{st}, 5^{th} and 10^{th}) of LFP@CNTs-10 h (Fig. 4a). It is noted that the gap

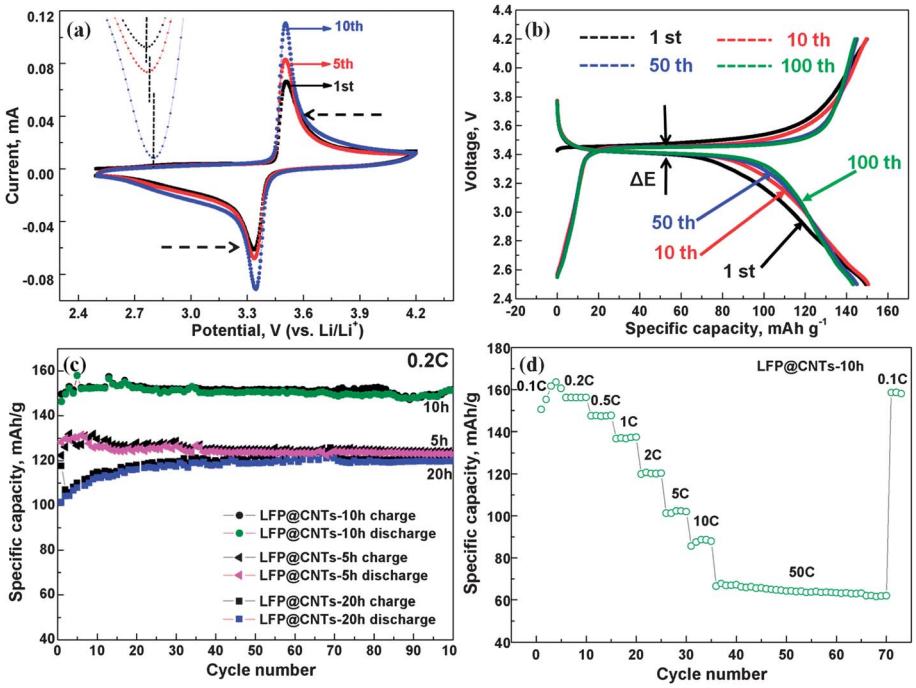

Fig. 4 (a) Cyclic voltammetry (CV) profiles for LFP@CNTs-10 at a scan rate of 0.1 mV s^{-1}. (b) Galvanostatic cycle charge–discharge profiles in the voltage range of 2.5–4.2 V at 0.2 C. (c) Cyclic performance at 0.2 C of composites annealed for different annealing times. (d) Rate capabilities of LFP@CNTs-10 nanocomposites.

between the redox peaks gradually decreases and the peak intensity increases in conjunction with the increase in cycle number (inset zoom in Fig. 4a), suggesting that the kinetics for lithium insertion and extraction are improved during cycling. The charge and discharge curves in different cycles (1st, 10th, 50th and 100th) show the same trend (Fig. 4b). The gap between the redox peaks becomes increasingly narrow from the initial cycle to the 100th cycle, and the value of the potential interval (ΔE) decreased from 83 mV in the initial cycle to 52 mV in the 10th cycle, 47 mV in the 50th cycle and 44 mV in the 100th cycle (Fig. S6†). LFP@CNTs-10 h nanocomposite delivers a discharge capacity of 155 mA h g^{-1} in the initial cycle at a current density of 34 mA g^{-1} (0.2 C), and the discharge capacity remains almost constant till 100 cycles.

The cycle performances of LFP@CNT composites at a current density of 34 mA g^{-1} (0.2 C) are shown in Fig. 4c. It is found that specific capacity does not fade over 100 cycles and the coulombic efficiency remains about 100%, demonstrating that LFP@CNT nanocomposites have an excellent cycling stability. Because of the amorphous CNT shell, LFP@CNTs-5 h delivers a capacity of 127 mA h g^{-1}. LFP@CNTs-20 h displays a capacity of 120 mA h g^{-1}, which is lower than that of LFP@CNTs-10 h, due to the agglomeration of $LiFePO_4$ nanorods and weak chemical bonding between the CNT shell and $LiFePO_4$ core. The discharge specific capacity of LFP@CNTs-10 h decreases from 160 to 102 mA h g^{-1} with an increasing current rate from a value of 0.1 C to 5 C regularly (Fig. 4d), and it still delivers a capacity of 65 mA h g^{-1} even at a high current density of 8500 mA g^{-1} (50 C, 1.2 minutes for charging and 1.2 minutes for discharging) with almost no fading up to 35 cycles, thereby indicating its high power performance. The results shown in Fig. 4b obviously demonstrate the remarkable electrochemical performance benefiting from the one dimensional core–shell LFP@CNT nanowire structure and 3D CNT network.

In summary, one-dimensional core–shell LFP@CNT nanowire composites are successfully synthesized *via* a facile sol–gel route followed by post-heating treatment. By using PMMA, the core–shell structure is obtained in the calcination step, and the structures display an encapsulated architecture with $LiFePO_4$ embedded inside and CNTs outside. The homogeneous CNT shells and 3D network act as a continuous conductive network since electrons are easily transferred between the surface of $LiFePO_4$ nanowires and CNTs. The small size of LFP nanowires confined by the polymer decreases the lithium ion diffusion path and increases the contact areas between the electrolyte and active materials; therefore, our LFP@CNT nanowires offer excellent cycling stability and rate capability. By conducting calcinations in argon, 10 h post-heating time is found to be optimal. Longer annealing time leads to agglomeration of $LiFePO_4$ nanorods and poor interaction with CNTs, resulting in poor electrochemical performance. In addition, the one dimensional core–shell nanostructures can be easily extended to other cathode or anode materials, and the performance of electrodes in lithium-ion batteries of electric or hybrid electric vehicles can then be optimized.

Acknowledgements

This work is supported by NSERC, Clariant (Canada) Inc. (former Phostech lithium Inc.), CRC Program and the University of Western Ontario.

References

1 A. K. Padhi, K. S. Nanjundaswamy and J. B. Goodenough, *J. Electrochem. Soc.*, 1997, **144**, 1188–1194.
2 N. Ravet, J. B. Goodenough, S. Besner, M. Simoneau, P. Hovington and M. Armand, *The Electrochemical Society and The Electrochemical Society of Japan, Meeting Abstracts*, Honolulu, HI, October 17–22, 1999, vol. 99-2.
3 A. Yamada, H. Koizumi, S.-I. Nishimura, N. Sonoyama, R. Kanno, M. Yonemura, T. Nakamura and Y. Kobayashi, *Nat. Mater.*, 2006, **5**, 357–360.
4 (*a*) J. Yang, J. Wang, D. Wang, X. Li, D. Geng, G. Liang, M. Gauthier, R. Li and X. Sun, *J. Power Sources*, 2012, **208**, 340–344; (*b*) J. Wang and X. Sun, *Energy Environ. Sci.*, 2012, **5**, 5163–5185; (*c*) J. Yang, J. Wang, X. Li, D. Wang, J. Liu, G. Liang, M. Gauthier, Y. Li, R. Li and X. Sun, *J. Mater. Chem.*, 2012, **22**, 7537–7543; (*d*) J. Wang, J. Yang, Y. Tang, R. Li, G. Liang, T.-K. Sham and X. Sun, *J. Mater. Chem. A*, 2013, **1**, 1579–1586.
5 K. Zaghib, A. Mauger, F. Gendron and C. M. Julien, *Chem. Mater.*, 2008, **20**, 462–469.
6 H. S. Zhou, D. L. Li, M. Hibino and I. Honma, *Angew. Chem.*, 2005, **117**, 807–812; *Angew. Chem., Int. Ed.*, 2005, **44**, 797–802.
7 (*a*) M. Gaberscek, R. Dominko and J. Jamnik, *Electrochem. Commun.*, 2007, **9**, 2778–2783; (*b*) R. Dominko, M. Bele, J. M. Goupil, M. Gaberscek, D. Hanzel, I. Arcon and J. Jamnik, *Chem. Mater.*, 2007, **19**, 2960–2969; (*c*) Y. S. Hu, Y. G. Guo, R. Dominko, M. Gaberscek, J. Jamnik and J. Maier, *Adv. Mater.*, 2007, **19**, 1963–1966.
8 V. Srinivasan and J. Newman, *J. Electrochem. Soc.*, 2004, **151**, A1517–A1529.
9 (*a*) P. S. Herle, B. Ellis, N. Coombs and L. F. Nazar, *Nat. Mater.*, 2004, **3**, 147–152; (*b*) Y.-H. Rho, L. F. Nazar, L. Perry and D. Ryan, *J. Electrochem. Soc.*, 2007, **154**, A283–A289.
10 S. W. Oh, S. Myung, S. Oh, K. H. Oh, K. Amine, B. Scrosati and Y. Sun, *Adv. Mater.*, 2010, **22**, 4842–4845.
11 A. A. Salah, A. Mauger, K. Zaghib, J. B. Goodenough, N. Ravet, M. Gauthier, F. Gendron and C. M. Julien, *J. Electrochem. Soc.*, 2006, **153**, A1692–A1701.
12 Y. Wu, Z. Wen and J. Li, *Adv. Mater.*, 2011, **23**, 1126–1129.
13 C. Sun, S. Rajasekhara, J. B. Goodenough and F. Zhou, *J. Am. Chem. Soc.*, 2011, **133**, 2132–2135.
14 S. Kim, J. Ryu, C. B. Park and K. Kang, *Chem. Commun.*, 2010, **46**, 7409–7411.
15 J. Liu, T. E. Conry, X. Song, M. M. Doeff and T. J. Richardson, *Energy Environ. Sci.*, 2011, **4**, 885–888.
16 Y. Zhou, J. Wang, Y. Hu, R. O'Hayreb and Z. Shao, *Chem. Commun.*, 2010, **46**, 7151–7153.
17 X. L. Wu, L. Y. Jiang, F. F. Cao, Y. G. Guo and L. J. Wan, *Adv. Mater.*, 2009, **21**, 2710–2714.

18 H. Liu, Y. Zhang, R. Li, X. Sun, D. Désilets and H. Abou-Rachid, *Carbon*, 2010, **48**, 1498–1507.
19 L. Cheng, X. L. Li, H. J. Liu, H. M. Xiong, P. W. Zhang and Y. Y. Xia, *J. Electrochem. Soc.*, 2007, **154**, A692–A697.
20 X. Lou and Y. Zhang, *J. Mater. Chem.*, 2011, **21**, 4156–4160.
21 M. M. Doeff, J. D. Wilcox, R. Kostecki and G. Lau, *J. Power Sources*, 2006, **163**, 180–184.
22 G. X. Wang, S. Bewlay, S. A. Needham, H. K. Liu, R. S. Liu, V. A. Drozd, J. F. Lee and J. M. Chen, *J. Electrochem. Soc.*, 2006, **153**, A25–A31.
23 K. Hsu, S. Hua, C. Chen, M. Cheng, S. Tsay, T. Chou, H. Sheu, J. Lee and B. Hwang, *J. Power Sources*, 2009, **192**, 660–667.
24 (*a*) J. Zhou, J. Wang, H. Fang and T. K. Sham, *J. Mater. Chem.*, 2011, **21**, 5944–5949; (*b*) J. Zhou, J. Wang, H. Fang, C. Wu, J. N. Cutler and T. K. Sham, *Chem. Commun.*, 2010, **46**, 2778–2780.
25 D. Wang, X. Li, J. Wang, J. Yang, D. Geng, M. Cai, R. Li, T. K. Sham and X. Sun, *J. Phys. Chem. C*, 2012, **116**, 22149–22156.